Nanoscale

PAPER

View Article Online
View Journal | View Issue

Cite this: *Nanoscale*, 2026, **18**, 5330

A surfactant-mediated Ni/MgAl bifunctional catalyst for highly selective tandem conversion of acetone to methyl isobutyl ketone

Zhongxu Zhang,[a] Shuangshuang Huang,[c] Jingya Sun,*[b] Qiang Yuan,*[a] Yan Zhu [a] and Xu Liu *[a]

Received 22nd October 2025,
Accepted 21st January 2026

DOI: 10.1039/d5nr04445f

rsc.li/nanoscale

Highly efficient conversion of acetone to methyl isobutyl ketone (MIBK) remains a challenging task due to the complicated reaction pathways. Herein, a surfactant-assisted impregnation strategy was developed to modify Ni/MgAl catalysts for acetone conversion. Interestingly, the introduction of surfactants can effectively modulate the catalyst acidity and basicity, thereby blocking the reaction pathway, leading to the isophorone by-product. Moreover, a sodium dodecyl sulfate (SDS) modified catalyst (Ni/MgAl-SDS) exhibited a Ni^{2+}-doped solid solution structure, as well as the conventional impregnated Ni/MgAl catalyst, while a sodium dodecylbenzene sulfonate (SDBS) modified catalyst (Ni/MgAl-SDBS) generated highly dispersed metallic nanoparticles with coexisting Ni^0/Ni^{2+} species. This unique structure efficiently drove the hydrogenation of a mesityl oxide intermediate, achieving a high MIBK selectivity of 94.5% in the acetone conversion process. This strategy provides a novel approach for the synergistic regulation of the metal state, acidity and basicity in tandem reactions.

Introduction

Methyl isobutyl ketone (MIBK) is a crucial high-performance solvent with wide applications in coatings, pharmaceuticals, and high-end chemical separations.[1–4] Currently, the industrial synthesis of MIBK containing multi-step processes heavily relies on noble metal catalysts (*e.g.*, Pd/UiO-66) and high energy consumption, leading to high production costs and low atom economy.[5–8] The one-pot direct conversion of acetone to MIBK is regarded as a promising alternative route due to the highly integrated reaction pathways and significantly improved atom utilization. Nevertheless, controlling the selectivity of this tandem process poses a serious problem: the key intermediate of mesityl oxide (MO), generated *via* aldol condensation of acetone, can either be hydrogenated on metal active sites to yield the targeted MIBK or more easily cyclized and dehydrogenated over strongly acidic and basic sites to form the by-product isophorone (IPH).[9,10] Indeed, the deep coupling between metal sites and acidic/basic sites in bifunctional catalysts leads to misdirection of competitive reaction pathways, which makes the precise design and effective regulation of active sites a critical challenge for the acetone-to-MIBK route. To meet the requirement for multifunctional active sites in the above reaction pathway, magnesium–aluminum hydrotalcite was selected as the precursor for the catalyst support, owing to its abundant surface acidic–basic sites, a characteristic that can be retained even after reduction treatment. Additionally, Ni was chosen as the active metal component due to its excellent hydrogenation activity and relatively low cost compared to noble metals.

The precise design of active sites in multifunctional catalysts lies in the direct control of metal–support interaction

[a]*State Key Laboratory of Coordination Chemistry, Key Laboratory of Mesoscopic Chemistry of Ministry of Education, School of Chemistry and Chemical Engineering, Nanjing University, Nanjing 210093, China*
[b]*School of Environmental Science, Nanjing XiaoZhuang University, Nanjing, 211171, China*
[c]*School of Physics and Technology, Wuhan University, Wuhan 430072, China*

Xu Liu

Xu Liu is a professor of physical chemistry at Jiangsu University. He obtained his B.S. from Shandong University in 2010 and Ph.D. in materials physics and chemistry from the University of Science and Technology of China in 2018. Then he worked as a postdoctoral researcher at Nanjing University from 2019 to 2024. His research interest focuses on the design, synthesis, and applications of atomically precise metal nanoparticles.

(MSI) strength.[11–14] While strong MSI can stabilize the Ni^{2+}-doped solid solution structures and suppress H_2 dissociation due to the downshift in the metal d-band centre caused by electron transfer, weak MSI facilitates the formation of highly active metallic Ni^0 nanoparticles. Surfactants with amphiphilic properties, leveraging their dynamic assembly at phase interfaces,[15,16] offer a new pathway for the cooperative regulation of MSI strength and acidic/basic site distribution: their hydrophilic head groups (*e.g.*, $-SO_3^{2-}$ and $-SO_4^{2-}$) directionally anchor metal precursor ions *via* electrostatic interactions, while their hydrophobic tails inhibit particle sintering during high-temperature calcination through steric hindrance; more importantly, the thermally decomposed surfactants can interact with the support, effectively reducing surface acidity and basicity. However, the existing research predominantly focuses on the roles of surfactants in improving metal dispersion and loading,[17–19] while a systematic understanding of their microscopic mechanisms remains unaddressed. Specifically, it is still unclear how the surfactant molecule precisely regulates the metal chemical state and acid/base strength through nano-interfacial engineering, particularly in the structure–activity relationship governing the path-directed regulation of tandem reactions.

This study proposes an innovative strategy based on regulating surfactant head group chemistry, which enables the dual optimization of metal hydrogenation functionality and acidic/basic sites through molecular design. Using sodium dodecyl sulfate (SDS) and sodium dodecylbenzene sulfonate (SDBS) to modify Ni/MgAl catalysts, head group-specific mechanisms were revealed: the benzene ring of SDBS enriches nickel precursors *via* hydrophobic interactions, inducing the formation of highly dispersed metallic Ni^0 nanoparticles; whereas the sulfate group of SDS strongly coordinates with the surface hydroxyl groups of the support, driving Ni^{2+} incorporation into the MgAl lattice to form a stable solid solution. Simultaneously, according to the results of CO_2 and NH_3-TPD, SDS and SDBS thermal decomposition significantly reduces the density of basic sites by 77% and 91%, respectively, and acidic sites by approximately 98% for both compared with a catalyst without surfactant modification, effectively inhibiting the IPH side reaction.[20] By using surfactants to cooperatively regulate metal sites and acidic and basic sites, this study successfully realizes the tandem pathway of acetone–MO intermediate-hydrogenation with the high selectivity of 94.5% for MIBK over the Ni/MgAl-SDBS catalyst, which is increased by more than 90% in comparison with the catalyst without surfactant modification.

Results and discussion

The reaction pathway selection for the conversion of acetone to MIBK is inherently determined by the precise regulation of the catalyst's interfacial microenvironment. As shown in Fig. 1, this reaction network contains a critical branching path: the intermediate MO, generated through acid/base-catalysed condensation, can undergo either hydrogenation on metal sites to

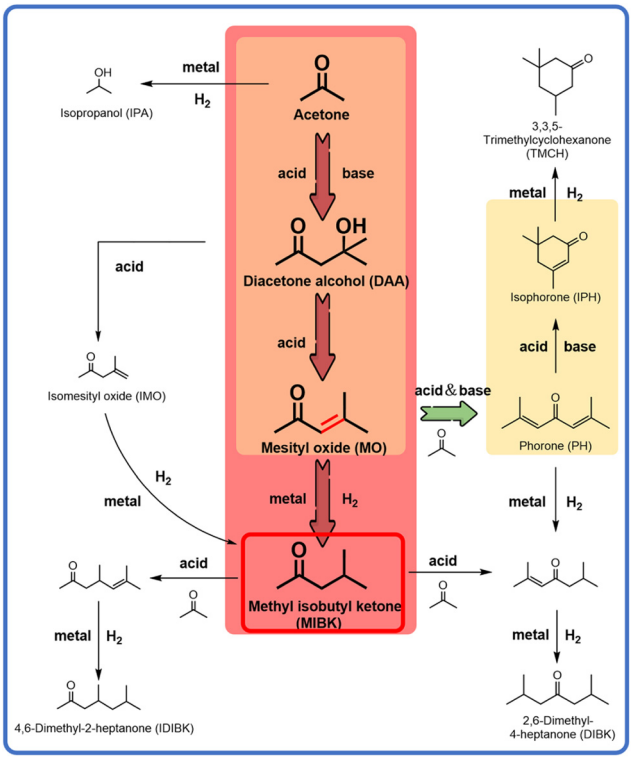

Fig. 1 The main reaction routes involved in the acetone conversion.

form the targeted MIBK or cyclization and dehydrogenation on acidic and basic sites to yield the by-product IPH.[20–23] This pathway competition stems from the intrinsic functional conflict between metal sites and acidic/basic sites: the efficient hydrogenation of MO requires highly active metallic Ni^0, while the suppression of IPH formation necessitates weakening of the strong acidity and basicity of the support; however, excessive reduction of acidity and basicity hinders the condensation step from acetone to MO. To resolve this contradiction, this study employs a surfactant strategy to regulate the surface properties of the MgAl hydrotalcite support. After using SDS and SDBS, the densities of acidic and basic sites are significantly reduced (Fig. S1), effectively inhibiting IPH generation while retaining adequate acidic and basic sites to maintain MO condensation activity, thereby enriching the MO intermediate. Subsequently, selective hydrogenation of MO catalysed by the loaded Ni particles ultimately enables highly selective conversion of acetone to MIBK.

Catalytic performances of three types of catalysts for acetone conversion and MIBK selectivity were tested and compared. As shown in Fig. 2a, the surfactants themselves exhibited no catalytic activity in acetone conversion, while MgAl was able to catalyse the condensation of acetone into the MO intermediate, further transforming into IPH with a high selectivity of 76.5%. This catalytic ability was mainly attributed to its inherent acid–base properties. After modification with SDBS, the activity of MgAl-SDBS decreased, and the selectivity for IPH dropped to 11.95%. It is speculated that the number of acidic and basic sites decreased after surfactant modification. After

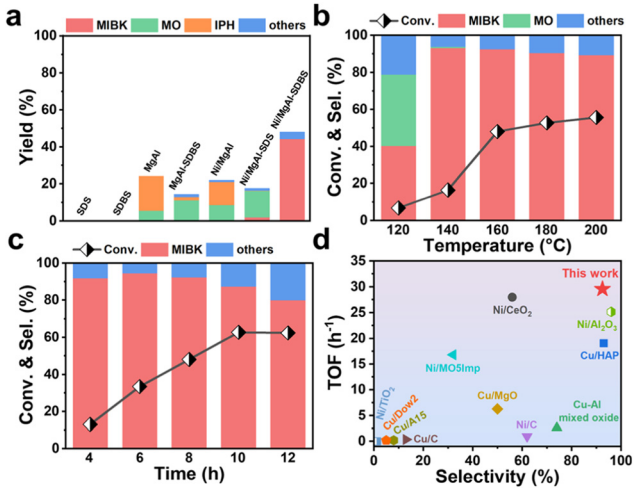

Fig. 2 (a) Catalytic performances of SDS, SDBS, MgAl, Ni/MgAl, Ni/MgAl-SDS, and Ni/MgAl-SDBS for acetone conversion. Reaction conditions: 160 °C, 4 MPa, 8 h, and 0.15 g catalyst. (b) Temperature-dependent and (c) time-dependent catalytic performances of the Ni/MgAl-SDBS catalyst. (d) The catalytic-performance comparison between Ni/MgAl-SDBS and non-noble metal catalysts previously reported in the conversion of acetone to MIBK.

the conventional impregnation of Ni element into the MgAl support, the main product for acetone conversion remained to be IPH, while the target product of MIBK was almost undetectable, indicating that Ni/MgAl could not get through the pathway of MO-MIBK (Fig. S2a). Interestingly, after the modification of SDS, the Ni/MgAl-SDS catalyst exhibited a high selectivity of 92.5% for MO (Fig. S2b), indicating that the acetone conversion stagnated at the MO stage and the subsequent pathway of MO-IPH was interrupted. Unfortunately, the alternative pathway of MO-MIBK was still inaccessible for the SDS-modified catalyst. Comparatively, when the surfactant of SDS was substituted by SDBS, the direct transformation of acetone to MIBK could be realized over the catalyst Ni/MgAl-SDBS. To verify the influence of surfactant dosage on catalyst performance, we varied the amount of SDBS used and evaluated the activity of the corresponding catalysts (Fig. S3). The results show that the amount of SDBS significantly affected the acetone conversion rather than the selectivity of MIBK. Hence, to ensure sufficient surfactant coverage during catalyst preparation, the SDBS : Ni molar ratio was set to be 10 : 1. After optimizing the reaction conditions, *e.g.*, temperature (Fig. 2b), reaction time (Fig. 2c), and H_2 pressure (Fig. S4), this catalyst exhibited a high selectivity of 92.5% for MIBK with an acetone conversion of 48.0%. The turnover frequency (TOF) of Ni/MgAl-SDBS for the reaction was calculated to be 29.54 h^{-1}. Notably, the overall catalytic properties of Ni/MgAl-SDBS are comparable to those of the best non-noble metal catalysts previously reported for the acetone conversion, as shown in Fig. 2d and Table S1.[24–32] We also conducted cycling performance tests on Ni/MgAl-SDBS (Fig. S5). The catalytic performance of Ni/MgAl-SDBS decreases rapidly with increasing cycle number. After two cycles, the acetone conversion decreased from 48.0% to 17.6%, and the selectivity to MIBK dropped from 92.45% to 45.30%.

By comparing the distinct performances of Ni/MgAl, Ni/MgAl-SDS, and Ni/MgAl-SDBS catalysts, it is rationally concluded that the surfactant incorporation could effectively influence the chemical composition and structure of the Ni/MgAl catalyst and thus significantly affect the reaction pathways for the transformation of acetone. To deeply understand the role of the surfactant, various characterization processes were carried out for the above catalysts. Initially, a N_2 adsorption–desorption test revealed that all three catalysts exhibited typical IV isotherms with H3-type hysteresis loops (Fig. 3a and S6).[33] In addition, the introduction of surfactants did not significantly change the surface area, pore volume and pore diameter of the catalyst (Table S2), reflecting that the incorporation of SDS and SDBS surfactants hardly affected the pore structure of MgAl oxides, which thus could ensure the mass transfer efficiency for the reactant during the catalytic process. X-ray diffraction (XRD) phase analysis showed that all samples exhibit typical hydrotalcite layered structure characteristics before reduction in H_2 at 450 °C.[34,35] In comparison, these signals experienced an obvious variation after the reduction process, indicating the formation of the corresponding metal oxides (Fig. 3b and S7). We also conducted XRD on Ni/MgAl-SDBS after the reaction (Fig. S8). The characteristic peaks of Ni particles were more obvious than those before the reaction, indicating that the Ni particles on the surface of the catalyst agglomerate under the reaction conditions, which might be the cause of catalyst deactivation.

Fourier transform infrared spectroscopy (FTIR) measurements were performed to characterize the variation of surfactants in the preparation of modified Ni/MgAl catalysts. As shown in Fig. 3c, the characteristic peak of the S=O stretching vibration of Ni/MgAl-SDBS centred at 1195 cm^{-1} disappeared after the H_2 reduction, implying the variation of the S element due to the breakage of S=O bonds. In contrast, this characteristic peak of Ni/MgAl-SDS remained after reduction, indicating that $-SO_4^{2-}$ could remain during the reduction process (Fig. S9).[36] In addition, the characteristic band in the 2848–2960 cm^{-1} region, corresponding to the stretching vibration of the C–H bond in $-CH_3$/$-CH_2-$ groups,[37] disappeared completely for both Ni/MgAl-SDBS and Ni/MgAl-SDS catalysts, verifying the removal of carbon tails due to surfactant decomposition during the reduction process. Scanning electron microscopy (SEM) and transmission electron microscopy (TEM) were performed to characterize the morphology of the catalysts. The SEM images showed typical characteristics of an oxide (Fig. 3d and S10), which were consistent with the XRD results.[38] As shown in Fig. 3e and f, some uniform and dispersed nickel nanoparticles were observed in the Ni/MgAl-SDBS catalyst, and the loading of Ni was determined to be 10.6 wt% (Table S4) by inductively coupled plasma optical emission spectroscopy (ICP-OES). Comparatively, this kind of nanoparticle was absent in the TEM images of both Ni/MgAl and Ni/MgAl-SDS (Fig. S11), indicating that Ni species mainly existed in solid solution to form

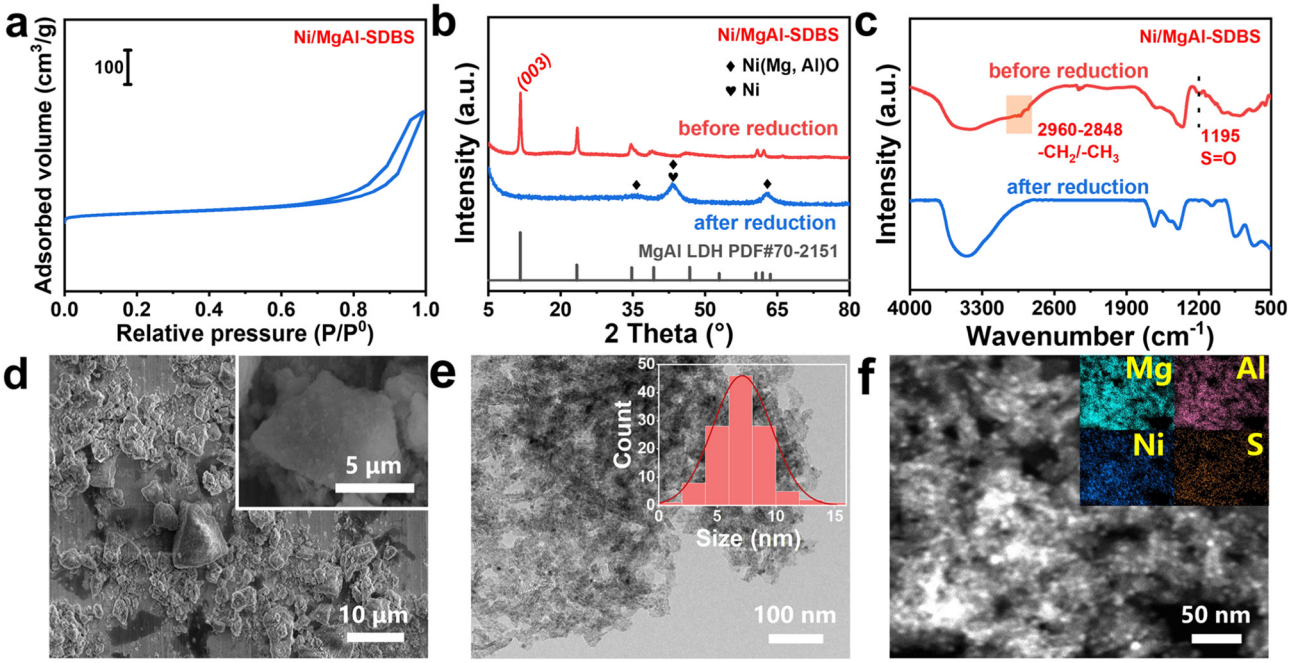

Fig. 3 (a) N_2 adsorption–desorption isotherms of Ni/MgAl-SDBS. (b) XRD patterns of Ni/MgAl-SDBS before and after reduction. (c) FTIR patterns of Ni/MgAl-SDBS before and after reduction. (d) SEM images of Ni/MgAl-SDBS. (e) TEM image of Ni/MgAl-SDBS. (f) TEM image and corresponding element mappings of Ni/MgAl-SDBS.

the oxide matrix. The Ni loadings were found to be 4.1% and 6.0% for Ni/MgAl and Ni/MgAl-SDS, respectively (Table S4). We conducted TEM tests on Ni/MgAl-SDBS after the reaction (Fig. S12). The results showed that the TEM images of the spent sample clearly showed a more pronounced agglomeration of Ni species, which is consistent with the results of XRD, verifying that the cause of catalyst deactivation is the agglomeration of active metals.

X-ray photoelectron spectroscopy (XPS) measurements were further carried out to detect the charge state of Ni and S elements. As depicted in Fig. S13a, the peak of Ni $2p_{3/2}$ was located at 855.63 eV for Ni/MgAl, agreeing well with the binding energy of Ni^{2+} ions, implying the sole existence of Ni^{2+} in the catalyst. For Ni/MgAl-SDS, the SDS modification did not affect the binding energy of Ni^{2+}, which might be ascribed to the enhanced electronic interaction between nickel and the support (Fig. 4a). For Ni/MgAl-SDBS, importantly, the peak of Ni $2p_{3/2}$ was negatively shifted to 855.08 eV, implying the variation of the valence state of Ni due to the incorporation of SDBS. Further profile fitting of the Ni $2p_{3/2}$ signal indicated that the ratio of Ni^0/Ni^{2+} species (BE: 854.50/855.63 eV) was approximately 1/1 (49.8%/50.2%) in the catalyst, which indicated that the nickel in Ni/MgAl-SDBS existed in mixed valence states.[39] These results are in line with the above TEM results and also demonstrate the significance of the Ni^0 species. As shown in Table S5, although both Ni/MgAl-SDS and Ni/MgAl-SDBS exhibit a reduction in the number of acidic sites compared to Ni/MgAl, only Ni/MgAl-SDBS shows a significant enhancement in MIBK selectivity. This indicates that merely reducing the acidity of the catalyst is insufficient to achieve

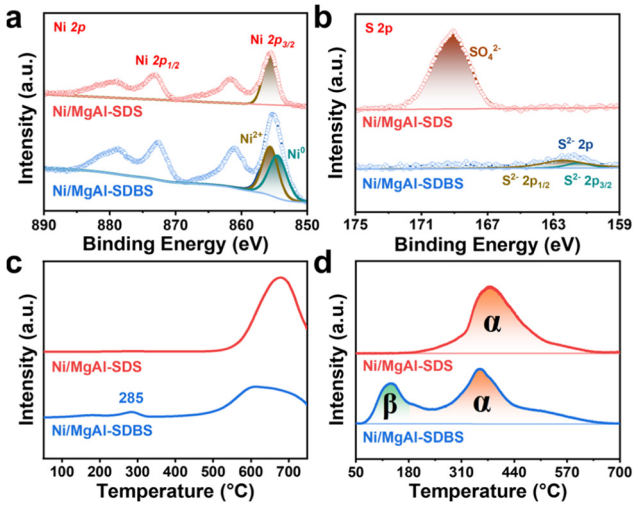

Fig. 4 (a) Ni 2p and (b) S 2p XPS profiles of Ni/MgAl-SDS and Ni/MgAl-SDBS catalysts. (c) H_2-TPR of Ni/MgAl-SDS and Ni/MgAl-SDBS catalysts. (d) H_2–D_2 exchange of Ni/MgAl-SDS and Ni/MgAl-SDBS catalysts.

high MIBK selectivity; it needs to simultaneously increase the proportion of Ni^0 species. These results further confirm the importance of synergistically regulating the metal state and acidic properties. In addition, the XPS data of S in Ni/MgAl-SDBS and Ni/MgAl-SDS catalysts revealed the variation of the surfactant in the preparation of the catalysts (Fig. 4b). Specifically, the binding energy of S 2p was around 162.0 eV in Ni/MgAl-SDBS, which could be assigned to S^{2-} species. This result further verified the breakage of $-SO_3^{2-}$ of SDBS during

the reduction process. In contrast, the signal of $-SO_4^{2-}$ was obviously detected in the XPS data of the Ni/MgAl-SDS catalyst, implying that the subsequent reduction process could not destroy the $-SO_4^{2-}$ anions. For the Ni and S in Ni/MgAl-SDBS and Ni/MgAl-SDS, the above differences mainly stemmed from the fundamental adsorption of SDBS and SDS on the support surface. Specifically, the benzene ring of SDBS might enrich $[Ni(H_2O)_6]^{2+}$ complexes *via* hydrophobic interactions and van der Waals forces, and weak MSI could facilitate the nucleation and growth of Ni^0 nanoparticles under H_2 reduction, whereas the O in $-SO_4^{2-}$ of SDS could be strongly coordinated with Ni^{2+} with the formation of Ni–O bonds together with surface hydroxyl groups of the support, which thereby inhibited the aggregation of Ni^{2+} ions and their subsequent reduction. To further illustrate the dispersion state of Ni on the surfaces of Ni/MgAl, Ni/MgAl-SDS and Ni/MgAl-SDBS, we conducted FT-IR for CO adsorption on the three catalysts (Fig. S14). For Ni/MgAl and Ni/MgAl-SDS, the characteristic peak of gaseous CO (2171 cm^{-1}) gradually disappeared after N_2 purging, leaving only the peak corresponding to linearly adsorbed CO on Ni^{2+} species (2175 cm^{-1}).[40] In contrast, for Ni/MgAl-SDBS, in addition to the linearly adsorbed CO peak on Ni^{2+} at 2178 cm^{-1}, a shoulder peak at 2162 cm^{-1} was observed, which is attributed to linearly adsorbed CO on Ni^0 species. These data are consistent with our previous TEM and XPS results, further demonstrating that Ni is uniformly dispersed within the support in Ni/MgAl and Ni/MgAl-SDS, whereas in Ni/MgAl-SDBS, Ni not only exists in the bulk phase but also aggregates on the surface to form particles.

Hydrogen temperature program reduction (H_2-TPR) further revealed the surfactant's influence on the reduction of Ni^{2+} to Ni^0. As depicted in Fig. 4c, the H_2-TPR profile of Ni/MgAl-SDBS showed a distinct reduction peak at 285 °C, corresponding to the nickel conversion from the ionic state to metallic state.[41,42] This low-temperature reduction capability for the Ni/MgAl-SDBS catalyst should be attributed to the weak MSI in the SDBS-modified system. In contrast, the reduction peak of Ni^{2+} in the bulk phase of Ni/MgAl-SDS significantly shifted to 650 °C, as the strong SMSI in the SDS-modified system made the reduction of Ni^{2+} more difficult.[43,44] This phenomenon is consistent with that of unmodified Ni/MgAl (Fig. S15a). More compelling support comes from H_2–D_2 isotope exchange experiments: the temperature for the maximum signal of HD was 130 °C for Ni/MgAl-SDBS (Fig. 4d). This low-temperature activity could be attributed to the excellent hydrogen dissociation capability of metallic Ni^0;[45] whereas the activation temperature surged to 380 °C for Ni/MgAl-SDS and to 425 °C for Ni/MgAl (Fig. S15b). The above characterization processes collectively demonstrated that the SDBS modification significantly promoted the reaction kinetics of hydrogen activation by facilitating the formation of metallic Ni^0.

Based on *in situ* Fourier transform infrared spectroscopy (*in situ* FTIR), we proposed a selective regulation mechanism of the reaction pathway for the acetone conversion on different catalysts. As shown in Fig. S16, for both Ni/MgAl-SDS and Ni/MgAl-SDBS samples, the prominent peak of 1738 cm^{-1} was assigned to the C=O group from physically adsorbed acetone, the intensity of which gradually decreased with the purging of N_2. Meanwhile, the characteristic peak of 1704 cm^{-1} hardly altered in intensity, and corresponded to the C=O group chemically adsorbed to acetone.[46] In addition, the characteristic peaks representing O–H (1645 cm^{-1}) were detected.[47] These results indicated that acetone combined with the two catalysts in the form of hydroxyl groups.[48] Considering the pathways of acetone transformation, it is concluded that the main difference in the reaction mechanism over Ni/MgAl-SDS and Ni/MgAl-SDBS lies in the subsequent steps after the generation of MO intermediates. Specifically, the Ni^{2+} ions in Ni/MgAl-SDS cannot effectively dissociate H_2, blocking the hydrogenation pathway of MO to MIBK; in contrast, the metallic Ni sites in Ni/MgAl-SDBS not only efficiently dissociate H_2 but also modulate the strength of adjacent acidic sites (maintain-

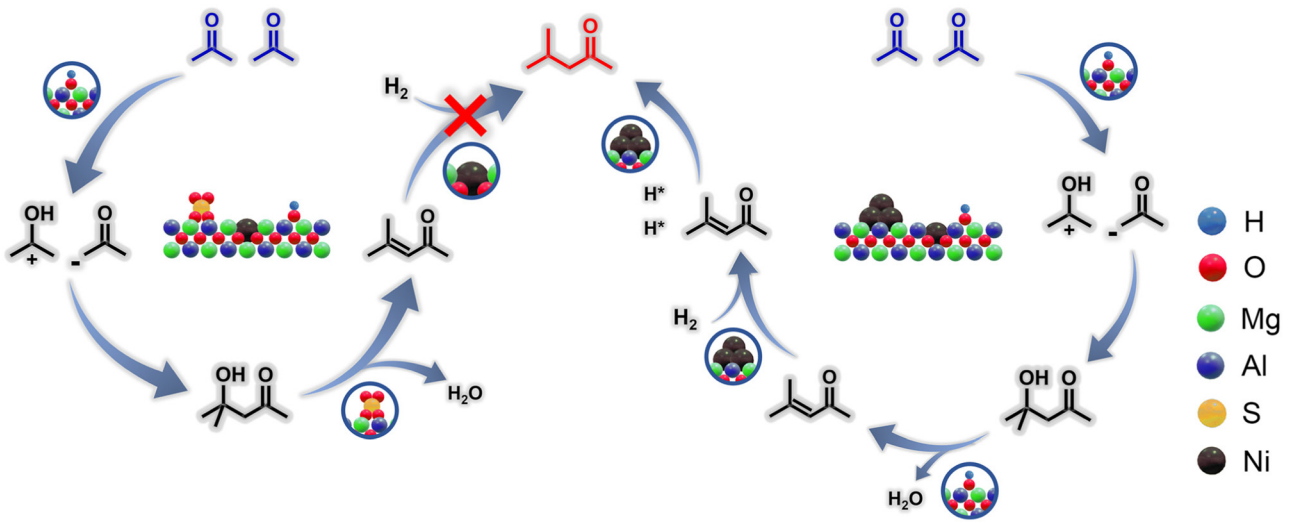

Fig. 5 Proposed reaction mechanisms of the acetone conversion on Ni/MgAl-SDS and Ni/MgAl-SDBS catalysts.

ing them at a moderately weak level) through electronic effects, thereby achieving an efficient synergy between MO adsorption and H* migration and thus promoting the highly selective formation of MIBK (Fig. 5).

Conclusions

This study successfully demonstrates the highly selective synthesis of methyl isobutyl ketone from acetone through a surfactant head group chemistry regulation strategy. Research showed that the hydrophobic region of the benzene ring in sodium dodecylbenzene sulfonate enriched nickel precursors *via* van der Waals forces, forming highly dispersed Ni^0 nanoparticles (5–8 nm) under moderate metal–support interactions; whereas the sulfate group of sodium dodecyl sulfate strongly coordinated with the support and stabilized the nickel species in the Ni^{2+} solid solution state. The thermal decomposition process of surfactants simultaneously reduced the density of acidic and basic sites on the catalyst surface, effectively inhibiting the isophorone side reaction pathway. In terms of catalytic performance, Ni/MgAl-SDBS demonstrates significant advantages: at a reaction temperature of 160 °C and an acetone conversion of 48.0%, MIBK selectivity reaches 92.5%. Mechanistic studies further indicate that the Ni^0 species possess efficient H_2 dissociation capability, thereby enabling the selective hydrogenation of the C=C bond in the intermediate mesityl oxide. This research provides new insights into the synergistic regulation of metal, acidic and basic sites in multi-step tandem reactions.

Author contributions

Xu Liu and Yan Zhu conceptualized this study. Zhongxu Zhang carried out the experimentation. Shuangshuang Huang focused on TEM analysis. Zhongxu Zhang, Jingya Sun and Qiang Yuan analysed and validated the experimental data. All authors drafted and reviewed the manuscript.

Conflicts of interest

There are no conflicts to declare.

Data availability

The data supporting this article have been included as part of the supplementary information (SI). Supplementary information: Fig. S1–S16, Tables S1–S6, and further experimental details. See DOI: https://doi.org/10.1039/d5nr04445f.

Acknowledgements

We are thankful for the financial support from the National Natural Science Foundation of China (22575104, 22125202, 92461312, and U24A20487) and SINOPEC Research Institute of Petroleum Processing Co., Ltd.

References

1 B. H. Juárez, D. Golmayo, P. A. Postigo and C. López, *Adv. Mater.*, 2004, **16**, 1732–1736.
2 N. Matsuhisa, D. Inoue, P. Zalar, H. Jin, Y. Matsuba, A. Itoh, T. Yokota, D. Hashizume and T. Someya, *Nat. Mater.*, 2017, **16**, 834–840.
3 X. Zhang, D. Zhang, Z. Sun, L. Xue, X. Wang and Z. Jiang, *Appl. Catal., B*, 2016, **196**, 50–56.
4 P. Nguyen, H. T. Ng and M. Meyyappan, *Adv. Mater.*, 2005, **17**, 549–553.
5 Y. Hu, Y. Mei, B. Lin, X. Du, F. Xu, H. Xie, K. Wang and Y. Zhou, *RSC Adv.*, 2021, **11**, 48–56.
6 R. Ma, Y. Li, G. Wu, Y. He, J. Feng, Y. Zhao and D. Li, *Chin. J. Catal.*, 2018, **39**, 1384–1394.
7 F. Alwadaani, E. Kozhevnikova and I. Kozhevnikov, *J. Catal.*, 2008, **257**, 199–205.
8 P. Wang, S. Bai, J. Zhao, P. Su, Q. Yang and C. Li, *ChemSusChem*, 2012, **5**, 2390–2396.
9 L. Faba, E. Díaz and S. Ordóñez, *Appl. Catal., B*, 2013, **142–143**, 387–395.
10 B. Lu, Z. Wang, S. Ma, S. Mao, Z. Chen and Y. Wang, *Chem Catal.*, 2021, **1**, 1449–1465.
11 T. Wang, J. Hu, R. Ouyang, Y. Wang, Y. Huang, S. Hu and W.-X. Li, *Science*, 2024, **386**, 915–920.
12 T. W. Van Deelen, C. H. Mejía and K. P. De Jong, *Nat. Catal.*, 2019, **2**, 955–970.
13 L. Gloag, S. V. Somerville, J. J. Gooding and R. D. Tilley, *Nat. Rev. Mater.*, 2024, **9**, 173–189.
14 P. Wu, S. Tan, J. Moon, Z. Yan, V. Fung, N. Li, S.-Z. Yang, Y. Cheng, C. W. Abney, Z. Wu, A. Savara, A. M. Momen, D. Jiang, D. Su, H. Li, W. Zhu, S. Dai and H. Zhu, *Nat. Commun.*, 2020, **11**, 3042.
15 B. Wang, B. Yin, Z. Zhang, Y. Yin, Y. Yang, H. Wang, T. P. Russell and S. Shi, *Angew. Chem., Int. Ed.*, 2022, **61**, e202114936.
16 Y. Li, Q. Zhang, Z. Dai, R. Wang, Z. Li, Y. Huang, R. Lai, F. Wei and F. Shao, *Adv. Sci.*, 2025, 2501580.
17 X. Zhang, Y. Zhao and C. Xu, *Nanoscale*, 2014, **6**, 3638.
18 Y. Wang, P. Liu, K. Zhu, J. Wang and J. Liu, *Nanoscale*, 2017, **9**, 14979–14989.
19 W. Zhan, Y. Shu, Y. Sheng, H. Zhu, Y. Guo, L. Wang, Y. Guo, J. Zhang, G. Lu and S. Dai, *Angew. Chem., Int. Ed.*, 2017, **56**, 4494–4498.
20 L. Faba, E. Díaz and S. Ordóñez, *Appl. Catal., B*, 2013, **142–143**, 387–395.
21 V. Yu. Kirsanov, L. F. Korzhova, S. G. Karchevskii, O. S. Travkina, B. I. Kutepov and N. G. Grigor'eva, *Ind. Eng. Chem. Res.*, 2025, **64**, 14395–14406.
22 S. K. Bej and L. T. Thompson, *Appl. Catal., A*, 2004, **264**, 141–150.

23 F. Liguori, C. Oldani, L. Capozzoli, N. Calisi and P. Barbaro, *Appl. Catal., A*, 2021, **610**, 117957.
24 K. Grzelak, M. Trejda and A. Riisager, *ChemSusChem*, 2022, **15**, e202102012.
25 V. Chikán, Á. Molnár and K. Balázsik, *J. Catal.*, 1999, **184**, 134–143.
26 E. Canadell, J. H. Badia, R. Soto, J. Tejero, R. Bringué and E. Ramírez, *Top. Catal.*, 2025, **68**, 59–81.
27 G. Waters, O. Richter and B. Kraushaar-Czarnetzki, *Ind. Eng. Chem. Res.*, 2006, **45**, 6111–6117.
28 J. Quesada, L. Faba, E. Díaz and S. Ordóñez, *J. Catal.*, 2019, **377**, 133–144.
29 A. C. C. Rodrigues, J. L. F. Monteiro and C. A. Henriques, *C. R. Chim.*, 2009, **12**, 1296–1304.
30 S. Narayanan and R. Unnikrishnan, *Appl. Catal., A*, 1996, **145**, 231–236.
31 S. Basu, J. J. Sarkar and N. C. Pradhan, *Catal. Today*, 2022, **404**, 182–189.
32 P. V. R. Rao, V. P. Kumar, G. S. Rao and K. V. R. Chary, *Catal. Sci. Technol.*, 2012, **2**, 1665.
33 F. Li, Y. Zhao, Y. Liu, Y. Hao, R. Liu and D. Zhao, *Chem. Eng. J.*, 2011, **173**, 750–759.
34 S. Kwon, J. Zhang, R. Ganganahalli, S. Verma and B. S. Yeo, *Angew. Chem.*, 2023, **135**, e202217252.
35 J. Hwang, H. M. Kim, S. Shin and Y. Sun, *Adv. Funct. Mater.*, 2018, **28**, 1704294.
36 C. Gong, C. Zhang, Q. Zhuang, H. Li, H. Yang, J. Chen and Z. Zang, *Nano-Micro Lett.*, 2023, **15**, 17.
37 P. Sanati-Tirgan, H. Eshghi and A. Mohammadinezhad, *Nanoscale*, 2023, **15**, 4917–4931.
38 D. Li, R. Li, M. Lu, X. Lin, Y. Zhan and L. Jiang, *Appl. Catal., B*, 2017, **200**, 566–577.
39 J. Tian, P. Zheng, T. Zhang, Z. Han, W. Xu, F. Gu, F. Wang, Z. Zhang, Z. Zhong, F. Su and G. Xu, *Appl. Catal., B*, 2023, **339**, 123121.
40 K. Hadjiivanov, H. Knözinger and M. Mihaylov, *J. Phys. Chem. B*, 2002, **106**, 2618–2624.
41 F. Minette, M. Lugo-Pimentel, D. Modroukas, A. W. Davis, R. Gill, M. J. Castaldi and J. De Wilde, *Appl. Catal., B*, 2018, **238**, 184–197.
42 Z. Zou, Y. Shen, C. Chen, W. Li, Y. Zhang, H. Zhang, Z. Yu, H. Zhao and G. Wang, *Adv. Funct. Mater.*, 2025, **35**, 2417584.
43 X. Zhai, H. Kang, X. Liu, W. Chu and Y. Liu, *Chem. Eng. J.*, 2025, **507**, 160151.
44 D. Li, L. Wang, M. Koike, Y. Nakagawa and K. Tomishige, *Appl. Catal., B*, 2011, **102**, 528–538.
45 T. Fu, P. Hu, T. Wang, Z. Dong, N. Xue, L. Peng, X. Guo and W. Ding, *Chin. J. Catal.*, 2015, **36**, 2030–2035.
46 K. Liu, Y. Sun, J. Feng, Y. Liu, J. Zhu, C. Han, C. Chen, T. Bao, X. Cao, X. Zhao, Y. Yang and G. Zhao, *Chem. Eng. J.*, 2023, **454**, 140059.
47 H. Alalwan and A. Alminshid, *Spectrochim. Acta, Part A*, 2020, **229**, 117990.
48 V. K. Díez, J. I. Di Cosimo and C. R. Apesteguía, *Appl. Catal., A*, 2008, **345**, 143–151.